

PAPER

Yellow light privacy protection with anti-reflection structure based on photonic band gap principle

To cite this article: Na Pei *et al* 2024 *J. Opt.* **26** 065104

View the [article online](#) for updates and enhancements.

You may also like

- [Enhancement of torque density and power density of polymer-based ultrasonic motors via flexible usage of anisotropy in elastic property](#)
Jinshuo Liu, Jiang Wu, Xing Gao et al.
- [Timing system design and tests for the Gravity Probe B relativity mission](#)
J Li, G M Keiser, J M Lockhart et al.
- [Moisture and temperature influence on mechanical behavior of PPS/buckypapers carbon fiber laminates](#)
J A Rojas, L F P Santos, M L Costa et al.

Yellow light privacy protection with anti-reflection structure based on photonic band gap principle

Na Pei¹, Bao-Fei Wan², Sun-Xin Xie², Ting-Hao Zhang² and Hai-Feng Zhang^{2,*} 

¹ School of Integrated Circuit Science and Engineering, Nanjing University of Posts and Telecommunications, Nanjing 210023, People's Republic of China

² College of Electronic and Optical Engineering & College of Flexible Electronics (Future Technology), Nanjing University of Posts and Telecommunications, Nanjing 210023, People's Republic of China

E-mail: hanlor@163.com and hanlor@njupt.edu.cn

Received 29 December 2023, revised 17 April 2024

Accepted for publication 3 May 2024

Published 14 May 2024



Abstract

This paper delves into the one-dimensional photonic crystals (PCs) privacy protection structure (PPS), emphasizing a layered structure with polarization-independent angular response characteristics tailored to meet the need for PPS in various situations. Introducing a specialized design for photonic band gap (PBG), the PPS adheres to the principles of PBG. This design comprises a host structure and an anti-reflection structure carefully selected within the yellow light band (frequency range spans from 530 THz to 510 THz). The given PPS creates an angle selection (AS) window exhibiting transmittance consistently above 0.85 within -29° to 29° while ensuring transmittance drops to 0.1 within the -90° to -46° and 46° – 90° range. This arrangement effectively achieves the desired PPS. The effects of the host structure on the four key parameters of refractive index and thickness of the two media on PPS properties were studied in detail. The influence of these parameters mainly involves the transmittance of the visible area, the AS, and the transmittance of the protected area.

Keywords: photonic crystals, photonic band gap, angle selection, privacy protection, yellow light

1. Introduction

Nowadays, information has become integral to daily life. An increasing number of individuals find themselves compelled to use electronic devices in environments devoid of adequate protection, either due to job demands or specific requirements [1–3]. However, in such open settings, ensuring that individuals can utilize electronic products without external interference, be it intentional or unintentional snooping, proves challenging through infrastructure alone [4, 5]. The most optimal solution, therefore, lies in addressing the issue directly at the screen level of electronic devices. The initial attempts at anti-snooping measures primarily involved ultra-fine shutter technology [6]. However, these methods exhibited

several shortcomings. The anti-snooping device design originates from the concept of subjecting the computer screen to extraordinary processing, ensuring it illuminates solely for the user and remains impervious to external ‘borrowing’ by unauthorized individuals. This concept finds application in a broad spectrum of areas, ranging from banking equipment like automatic teller machines to commonly used consumer electronics such as mobile phones and laptops [3, 4]. Responding to the increasing market demand, angle-controllable display screens have emerged as a focal point and a recent research direction for major display companies [1, 3]. Currently, two prevalent technical features address this issue: one way is surface-based display solutions [7–9]. This involves applying a solid adhesive or a physical card with an anti-glimpse film. The core technology often centers around ultra-fine shutter optical technology. In 2021, Li and Zhang introduced a polaroid structure with a narrow viewing angle function. The innovation lay in

* Author to whom any correspondence should be addressed.

replacing the upper protective layer in the polaroid with an anti-snooping film devoid of pressure-sensitive adhesive [10]. The other way is liquid crystal display (LCD) angle adjustment [11, 12]. Display solutions achieved by modifying the LCD angle width have also been proposed. In 2019, Chen *et al* suggested an anti-voyeurism display scheme utilizing a double-layer LCD screen framework [13]. This approach disrupts the display content at various viewing angles, effectively achieving anti-voyeurism objectives [14, 15].

Previous research in privacy protection structure (PPS) includes various methods such as textured glass [16], liquid crystal smart windows [17], double-response hydrogel electrochromism [18], tunnel transmission windows [19], light management films made of natural polymers with adjustable fog properties [20], liquid crystal asymmetric transmission windows [21, 22], among others. However, the conventional anti-snooping designs suffer from two major drawbacks. Firstly, due to inherent structural limitations, the transmission rate often falls below 70%, leading to darker screens that may impact eye health [21, 22]. Secondly, the transition range from the visible area to the protected area is substantial, approximately 20° , thereby compromising the efficacy of PP. Moreover, most anti-peep structures on the market offer a limited viewing range of -20° to 20° , further restricting their usability [7].

The core of privacy devices lies in effective angle selection (AS). Currently, three major principles govern this selection process. Three types of AS based on the photonic crystals (PCs) principle include the Brewster angle, photonic band gap (PBG), and gradient epsilon-near-zero (ENZ). First is the Brewster angle, where in 2014, Shen *et al* utilized the Brewster angle mode to achieve wide-band AS for TM wave, albeit without AS for TE case [14]. The second principle revolves around the PBG, aiming to impede light propagation within a specified range. In 2016, Iizuka *et al* introduced a region with very small wave vector dispersion in one-dimensional (1D) PCs heterostructures to achieve AS [23]. The last principle involves gradient ENZ. In 2021, Xu *et al* designed two wide screen directional transmitters using ENZ to achieve high emissivity within a specific angle range [24]. In recent years, scholars have proposed diverse designs to explore optimal angular selection structures, encompassing Brewster angle [14], anisotropic metamaterial [25], metamaterials [26], Fabry–Perot resonance [27], and PCs [28], among others. Currently, the PCs structure stands out as the most extensively studied, offering a more ideal AS. The Brewster angle displays a singular wavelength dependency and exclusively reflects TM waves. Moreover, in multi-layered dielectric systems, such as optical components with intricate coatings, the Brewster angle may be subject to the influence of multiple layer interfaces. ENZ materials have the drawbacks of high preparation difficulty, wavelength dependence, optical losses, material selection constraints, and engineering complexity. PBG exhibits frequency selectivity and tunable PBG width. In this material, optical waves are unable to propagate within a specific frequency range, known as the PBG, while propagation is allowed at other frequencies. The width of the PBG, typically adjustable by modifying the material's geometric structure or other parameters, demonstrates flexibility.

The human eye displays diminished sensitivity to yellow light, rendering it relatively well-adapted [29, 30], its application may impart a protective effect on the eyes, alleviating eye fatigue. In contrast to blue light, yellow light proves more effective in mitigating glare issues [31]. Moreover, yellow light exhibits lower energy levels, leading to decreased power consumption [32, 33], this is an advantage in environments emphasizing energy efficiency and environmental sustainability. Applying yellow light PP technology to screens, including those on electronic devices and digital billboards, aims to provide users with a gentler visual experience [29, 30]. This technology, whether on computer monitors or outdoor displays, helps reduce light pollution and enhances ambient lighting's positive impact on the environment [32, 33]. Additionally, in low-light or nighttime conditions, yellow light PPS technology minimizes glare, improving users' visual adaptability, making it advantageous for tasks like nighttime driving or aerospace activities [31].

The 1D PC consists of layers of materials with alternating refractive indices, exhibiting periodic changes in one direction. This structure creates a PBG for a specific range of wavelengths, preventing the propagation of light within that range. They are commonly used in the manufacture of optical filters and mirrors, among other optical devices [34]. The PBG refers to the band-like structure formed by the dispersion relation curves of electromagnetic waves under the modulation of the periodic refractive index of the PC. The gaps between these bands are called 'photonic band gaps'. Photons whose energy lies within these gaps cannot propagate through the PC [35].

Based on the PBG principle, introducing a novel 1D PCs designed to adhere to the display surface, providing anti-prying functionality. PPS we have devised allows for AS within the yellow light band, specifically in the frequency range of 510 THz–530 THz. Within the range of -29° to 29° , the transmittance consistently exceeds 0.9, while at angles ranging from -90° to -46° and 46° – 90° , the transmittance is deliberately reduced to 0.1. The designing PCs boasts high transmittance, and the transition angle range is limited to less than 20° . This innovation addresses the drawbacks of traditional anti-peep structures, overcoming the challenges of low transmittance and an extended visual range.

2. Model and numerical calculation method

In figure 1(a), devising PPS comprises an anti-reflection structure and a host structure. The PPS is composed of an anti-reflection structure and host structure. The anti-reflection layer consists of the red medium in the figure molybdenum diselenide ($n_D = 2.87$) [36] and blue media glass aerogel ($n_C = 1.08$) [37, 38] formed by cross-stacking each other, their thicknesses are respectively $d_{C1} = 96$ nm and $d_D = 106$ nm, and the number of layers of it is $m = 27$. The special thing is that for the anti-reflection structure located above, the thickness of the glass aerogel in the top layer is $d_{C2} = 48$ nm and for anti-reflection structures located underneath, the thickness of the glass aerogel in the lowest layer is $d_{C2} = 48$ nm. The

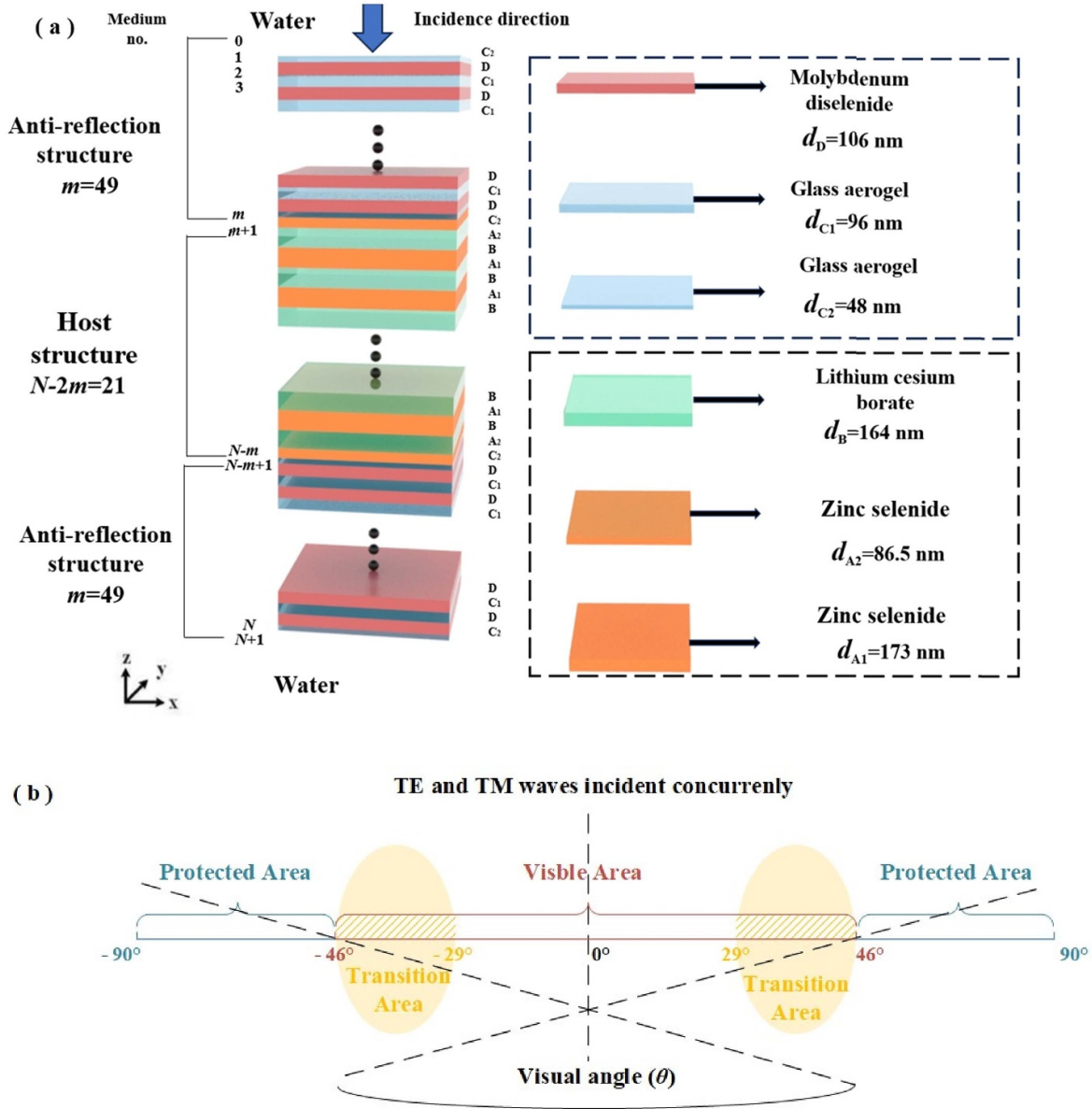


Figure 1. (a) The given PPS with the following parameters: refractive indices of $n_A = 2.63$, $n_B = 1.44$, $n_C = 1.08$, $n_D = 1.45$, $n_W = 1.33$; thicknesses of $d_A = 173$ nm, $d_B = 164$ nm, $d_C = 96$ nm, $d_D = 106$ nm; and a total number of layers $N = 119$, with the number of layers in the anti-reflection structure being $m = 49$. (b) Privacy protection effect.

main structure of the PPS is shown in green medium lithium cesium borate ($n_B = 1.44$) [39] and orange media zinc selenide ($n_A = 2.63$) [40], their thicknesses are $d_A = 173$ nm and $d_B = 164$ nm. Among them, the thickness of the zinc selenide in the uppermost and lowest layers of the host structure is half the thickness of the other zinc selenides $d_{A_1} = 86.5$ nm. The number of layers of the host structure is 21, and the number of layers of the PPS is 119. The total media arrangement of PPS is $C_2(DC_1)^{12}DC_2A_2(BA_1)^9BA_2C_2(DC_1)^{12}DC_2$. The surrounding of the entire PPS is water ($n_0 = 1.33$) [41].

For TE and TM waves incident along the $+z$ -axis on the PSS, visible and protected areas are formed. In figure 1(b), the black angular range (-90° to -46° and 46° – 90°) delineates the protected area, where transmittance is practically zero, rendering objects behind the PSS invisible. The red angular

range (-46° to 46°) denotes the visible area, demonstrating high transmittance within this angle range, enabling the observation of objects behind the structure. Within the visible area, a section of the yellow angular range (-46° to -29° and 29° – 46°) is defined as the transition area. In this angular range, certain frequencies in the yellow light spectrum exhibit high transmittance, while for other frequencies in the yellow light spectrum exhibit, transmittance is essentially zero. Concurrently, for specific angles within this range, both TM and TE waves display high transmittance, whereas for other angles within this range, the transmittance is essentially zero.

The energy transfer between dielectric layers can be calculated by the transfer matrix method (TMM) [42]. For each layer of dielectric, the transfer matrix can be described as (TE wave) [42]

$$\mathbf{M}_{TEi} = \begin{bmatrix} \cos \delta_{TEi} & -\frac{i}{\gamma_{TEi}} \delta_{TEi} \\ -i\gamma_{TEi} \sin \delta_{TEi} & \cos \delta_{TEi} \end{bmatrix} \quad (1)$$

$$\text{where, } \begin{cases} \delta_{TEi} = -\frac{\omega}{c} \sqrt{\varepsilon_i} \cos \theta_i \\ \gamma_{TEi} = \sqrt{\frac{\varepsilon_0}{\mu_0}} \sqrt{\varepsilon_i} \cos \theta_i \end{cases}$$

For each dielectric layer, the transfer matrix can be expressed in terms of TM wave characteristics [42],

$$\mathbf{M}_{TEi} = \begin{bmatrix} \cos \delta_{TEi} & -\frac{i}{\gamma_{TEi}} \sin \delta_{TEi} \\ -i\gamma_{TEi} \sin \delta_{TEi} & \cos \delta_{TEi} \end{bmatrix} \quad (2)$$

$$\text{where, } \begin{cases} \delta_{TEi} = -\frac{\omega}{c} \sqrt{\varepsilon_i} \cos \theta_i \\ \gamma_{TEi} = \sqrt{\frac{\varepsilon_0}{\mu_0}} \frac{\sqrt{\varepsilon_i}}{\cos \theta_i} \end{cases}$$

The characteristic matrix of the PC is [42],

$$\mathbf{M} = \begin{bmatrix} m_{11} & m_{12} \\ m_{21} & m_{11} \end{bmatrix} = \mathbf{M}_1 \mathbf{M}_2 \mathbf{M}_3 \cdots \mathbf{M}_N. \quad (3)$$

For either TE wave or TM one, the reflection and transmission coefficients can be expressed as, respectively [42],

$$r = \frac{(m_{11} + m_{12} \cdot \gamma_0) \gamma_0 - (m_{21} + m_{22} \cdot \gamma_0)}{(m_{11} + m_{12} \cdot \gamma_0) \gamma_0 + (m_{21} + m_{22} \cdot \gamma_0)} \quad (4)$$

$$t = \frac{2}{(m_{11} + m_{12} \cdot \gamma_0) \gamma_0 + (m_{21} + m_{22} \cdot \gamma_0)} \quad (5)$$

where for TM wave $\gamma_0 = \sqrt{\frac{\varepsilon_0}{\mu_0}} \frac{n_0}{\cos \theta}$ and for TE wave $\gamma_0 = \sqrt{\frac{\varepsilon_0}{\mu_0}} n_0 \cos \theta$, ε_0 is permittivity of vacuum, μ_0 is permeability of vacuum, n_0 is refractive index of water.

Thus, reflectance and transmittance can be represented separately [42],

$$R = |r|^2 \quad (6)$$

$$T = |t|^2. \quad (7)$$

We employ impedance matching theory for analysis. The normalized surface impedance is defined as the ratio of the impedance of the entire structure to the impedance of the vacuum wave, as detailed in [23] and [43],

$$\frac{Z_{\text{eff}}}{Z_0} = Z_{r,\text{eff}} + jZ_{i,\text{eff}} = \frac{1+r}{1-r}. \quad (8)$$

In this context, $Z_0 = |E_0|/|H_0| = \sqrt{(\mu_0/\varepsilon_0)}$ represents the vacuum wave impedance [23], with a typical value of approximately 377Ω [44, 45]. $Z_0 = |E_0|/|H_0| = \sqrt{(\mu_0/\varepsilon_0)}$ denotes the effective impedance of the PPS. Through analysis, optimal impedance matching occurs when the real and imaginary parts of the normalized surface impedance closely approach 1 and 0, respectively. This configuration minimizes reflection to the greatest extent.

3. Analysis and discussion

The PPS boasts a distinctive design, characterized by the incorporation of an anti-reflection layer. PPS media lacking this anti-reflection layer are structured as $A_2(BA_1)^9BA_2$. In figure 2(a), it is evident that PPS without the anti-reflection layer structure, operating at 510 THz, exhibits a remarkably high transmittance of TM waves (>0.85) in the protected area (angle range greater than 38° and less than -38°), with the transmittance of TE waves essentially at 0.1. A similar phenomenon is observed in figure 2(b) at 530 THz. To address this, devising an anti-reflection layer structure denoted as $C_2(DC_1)^{12}DC_2$. Incorporating this structure at both ends of $A_2(BA_1)^9BA_2$ results in a new PCs medium arrangement: $C_2(DC_1)^{12}DC_2A_2(BA_1)^9BA_2C_2(DC_1)^{12}DC_2$, constituting the final PPS. As depicted in figure 2(c), the addition of the anti-reflection layer structure results in the transmittance of TE and TM waves approaching 0.1 at angles greater than 37° and less than -37° . Meanwhile, the transmittance of TM and TE waves at angles from -29° to 29° is consistently above 0.9, with transition regions at -37° to -29° and 29° – 37° . The incident TM and TE waves on the PPS create an AS window of -37° to 37° , forming a visual area and effectively serving as PP. Similarly, at 530 THz in figure 2(d), an AS window ranging from -46° to 46° is established. At angles greater than 46° and less than -46° , the transmittance approaches 0.1, while at -36° to 36° , the transmittance is consistently above 0.85.

When the TE wave is incident on the PPS with the medium arrangement of $C_2(DC_1)^{12}DC_2A_2(BA_1)^9BA_2C_2(DC_1)^{12}DC_2$, the transmittance-angle relationship at 510 THz and 530 THz is depicted in figure 3(a). Transmittance approaches 0.1 at angles greater than 38° and less than -38° , while within the -29° to 29° angle range, the transmittance consistently exceeds 0.9. In figure 3(b), for TM waves incident on the same PPS structure, whether at 510 THz or 530 THz, the transmittance exceeds 0.85 within the -34° to 34° angle range and drops below 0.1 for angles greater than 46° and less than -46° . Figure 3(c) vividly demonstrates the AS effect at a wave frequency of 510 THz. A visible area is formed approximately from -38° to 38° , with transition areas at -38° to -29° and 29° – 38° , while angles greater than 38° and less than -38° constitute the protected area. In figure 3(d), with a wave frequency of 530 THz, a visible area is established from -46° to 46° , with transition areas at -46° to -38° and 38° to 46° , while angles greater than 46° and less than -46° form the protected area. In conclusion, for both TE and TM waves at 510 THz and 530 THz, the final visible region spans from -46° to 46° , encompassing transition areas from -46° to -29° and 29° – 46° angles greater than 46° and less than -46° constitute the protected area.

The PPS designed primarily employs the PBG principle [23]. The dispersion relation of 1D period is as follows [46]

$$\cos kd = \cos \delta_B \cos \delta_A - \frac{1}{2} \left(\frac{\eta_A}{\eta_B} - \frac{\eta_B}{\eta_A} \right) \sin \delta_B \sin \delta_A \quad (9)$$

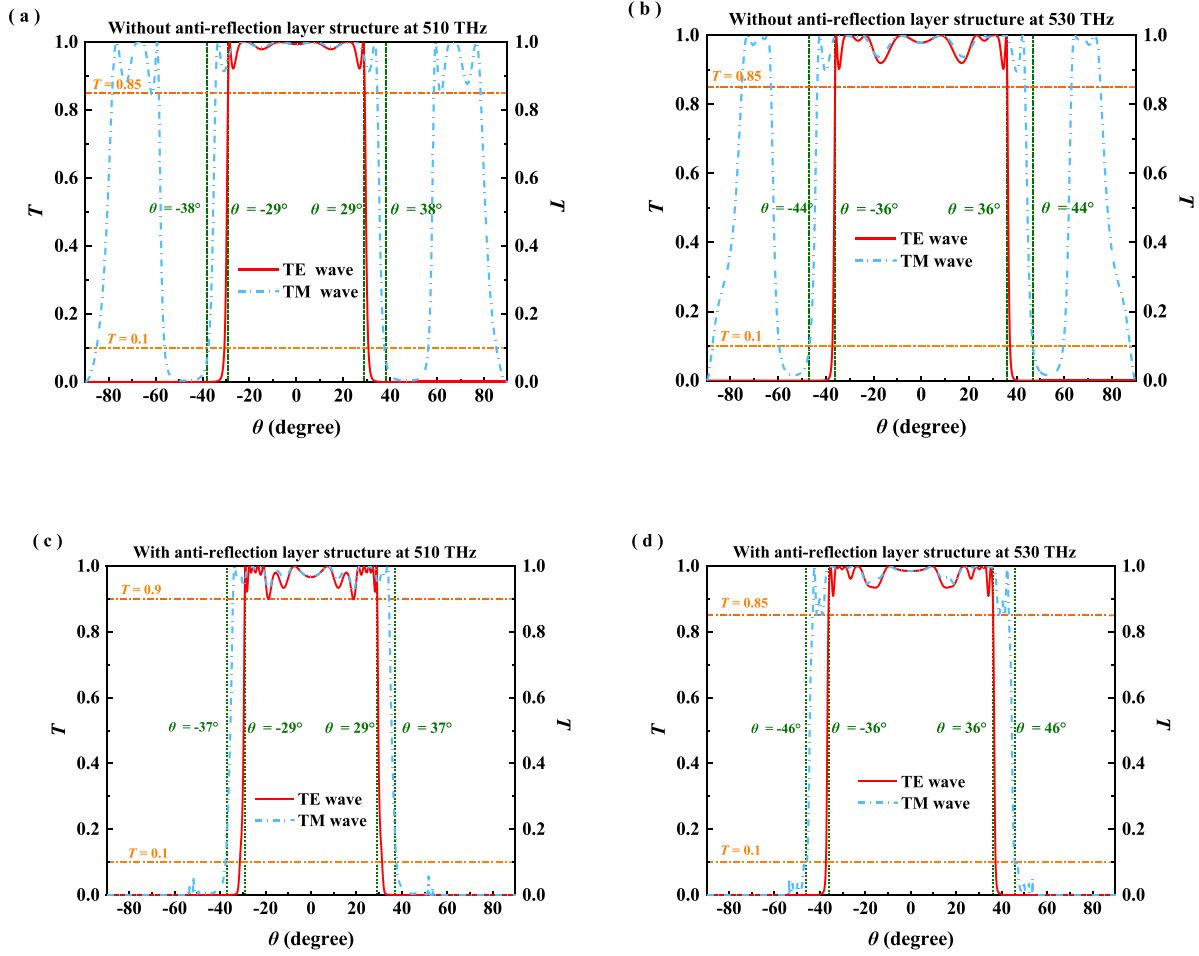


Figure 2. Relation between transmittance and angle, when PPS without the anti-reflection layer structure ($A_2(BA_1)^9BA_2$), (a) at 510 THz, and (b) at 530 THz. When PPS with the anti-reflection layer structure ($C_2(DC_1)^{12}DC_2A_2(BA_1)^9BA_2C_2(DC_1)^{12}DC_2$), (c) at 510 THz, and (d) at 530 THz. The blue line corresponds to a frequency of 530 THz, while the red line represents 510 THz.

where,

$$\left\{ \begin{array}{l} \delta_A = -\frac{\omega}{c} \sqrt{\varepsilon_A} d_A \cos \theta_A \\ \delta_B = -\frac{\omega}{c} \sqrt{\varepsilon_B} d_B \cos \theta_B \end{array} \right., \text{ for TE wave } \left\{ \begin{array}{l} \gamma_A = \sqrt{\frac{\varepsilon_0}{\mu_0}} \sqrt{\varepsilon_A} \cos \theta_A \\ \gamma_B = \sqrt{\frac{\varepsilon_0}{\mu_0}} \sqrt{\varepsilon_B} \cos \theta_B \end{array} \right. \text{ and for TM wave } \left\{ \begin{array}{l} \gamma_A = \sqrt{\frac{\varepsilon_0}{\mu_0}} \frac{\sqrt{\varepsilon_A}}{\cos \theta_A} \\ \gamma_B = \sqrt{\frac{\varepsilon_0}{\mu_0}} \frac{\sqrt{\varepsilon_B}}{\cos \theta_B} \end{array} \right.$$

Using the example of a TE wave at 530 THz, figure 4(a) illustrates that at the 30° viewing angle, when kd is greater than 0, indicating a state outside the PBG, there is transmittance. Similarly, at the 60° viewing angle with kd equal to 0, it signifies a position outside the PBG, resulting in transmittance. In figure 4(c), when the θ is 30°, the transmittance of the TE wave is present and exceeds 0.85. However, at 60°, the transmittance of the TE wave essentially approaches 0. For the TM wave, as shown in figure 4(b), at a -30° viewing angle, kd is greater than 0, allowing light transmission as it is not within

the band gap. In figure 4(c), transmittance is observed at 30°, exceeding 0.85. However, at 60°, where kd equals 0, it falls within the band gap, resulting in no transmission, consistent with the observed transmittance of 0° at 60° in figure 4(c). By observing the normalized impedance in figure (d), it can be found that for TM waves, the real part of the impedance basically tends to 1 and the imaginary part tends to 0 at about -46°-46°. Similarly for TE waves, the real part of the impedance tends to 1 and the imaginary part tends to 0 at about -38°-38°. The PPS structure can be seamlessly applied to the surfaces of

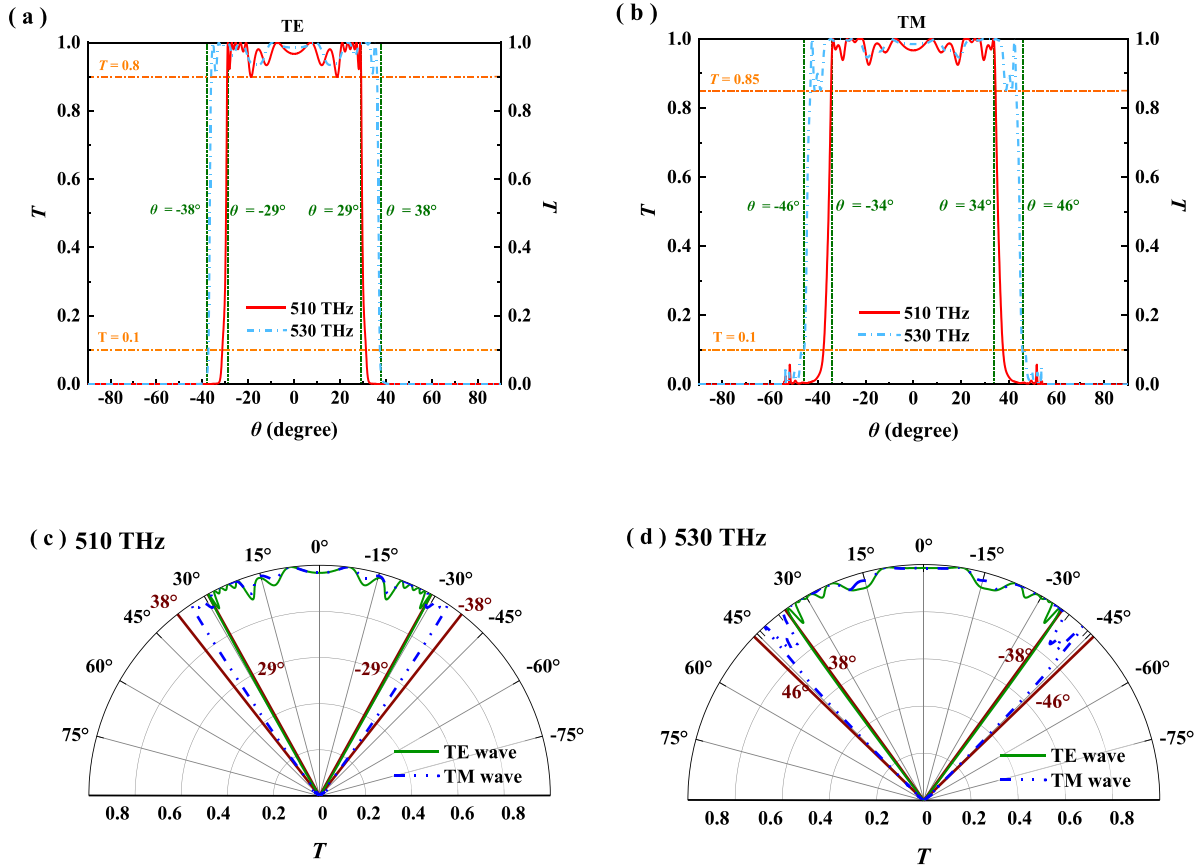


Figure 3. When PPS is $C_2(DC_1)^{12}DC_2A_2(BA_1)^9BA_2C_2(DC_1)^{12}DC_2$ illustrating the relationship between the angle and transmittance (a) TE wave incidence, and (b) TM wave incidence. Polar coordinates showcasing the angular transmittance relationship (c) at 510 THz, and (d) at 530 THz.

displays, images, or other information carriers. In the direction perpendicular to the PPS stack, background light is allowed to pass through, facilitating the observer’s view of the information. As the tilt angle increases, the visibility of the information gradually diminishes. When the angle between the tilt angle and the anti-snooping film plane reaches a specific value, the information becomes fully shielded. This prevents observers from other directions from accessing the information, ensuring robust PP.

Figure 5 explores the impact of n_A on PPS performance. As n_A decreases from 2.63 to 2.6, a gradual shrinkage of the visible region occurs within the 510–530 THz range. Taking 510 THz as an example, for TE waves, the visible region contracts from -29° – 29° to -25.9° – 25.9° . A similar trend is observed for TM waves, transitioning the visible region from -34° – 34° to -33.3° – 33.3° . Conversely, as n_A gradually increases to 2.73, the visible region expands. Using 530 THz as an example, for TE waves, the visible region expands from -38° – 38° to -39° – 39° . Similarly, for TM waves, the visible region broadens from -46° – 46° to -48° – 48° . Thus, an elevation in n_A gradually enlarges the visible region, while a reduction in n_A contracts the angle window.

The impact on n_B on the performance of the PPS is detailed in figure 6. As n_B decreases from 1.44 to 1.4, a gradual reduction in the visible region is evident across the 510–530 THz range. Using 510 THz as an illustration, for TE waves, the visible region contracts from -29° – 29° to -25.9° – 25.9° . Similar trends are observed for TM waves, with the visible region transitioning from -34° – 34° to -31.3° – 31.3° . Considering both TE and TM cases, the visible region shifts from -34° – 34° to -31.3° – 31.3° . Conversely, with n_B gradually increasing to 1.52, the visible region expands. Taking 530 THz as an example, for TE waves, the visible region expands from -38° – 38° to -38.7° – 38.7° and further extends to -42.1° – 42.1° . Similarly, for TM waves, the visible region broadens from -46° – 46° to -46.5° – 46.5° and further to -49.4° – 49.4° . Considering both TE and TM, the visible region expands from -46° – 46° to -46.5° – 46.5° and further to -49.4° – 49.4° . Consequently, an increase in n_B leads to a gradual enlargement of the visible region, while a decrease in n_B results in a reduction in the angle window.

Figure 7 delves into the impact of d_A on PPS performance. As d_A decreases from 173 nm to 170 nm, a gradual reduction in the visible region is observed within the 510–530 THz range. Using 530 THz as an example, for TE waves, the visible region contracts from -38° – 38° to -33.1° – 33.1° , and TM waves exhibit a similar phenomenon, with the visible region

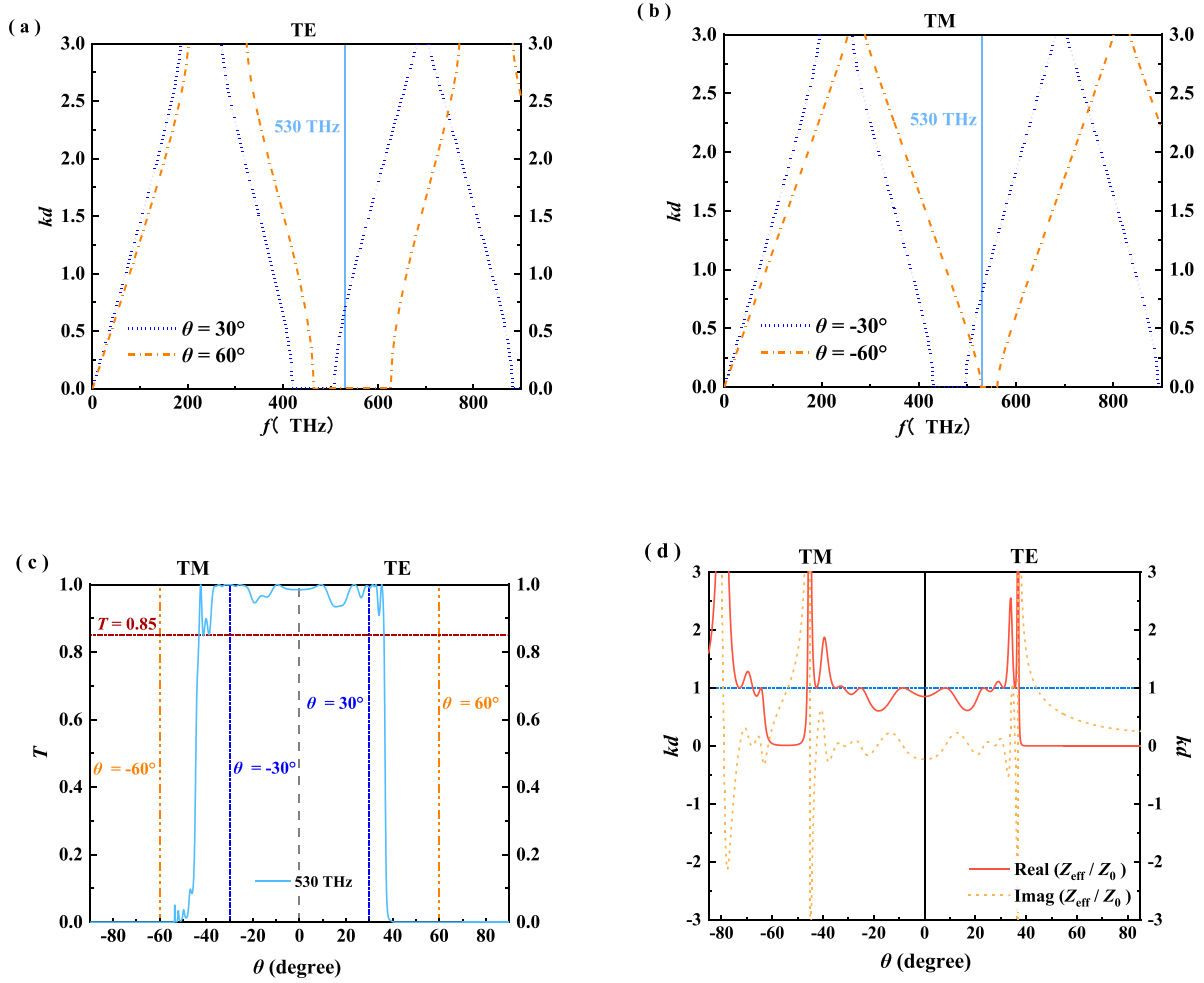


Figure 4. (a) Dispersion distribution of the PPS influenced by angle regulation under the TM wave. (b) Dispersion distribution of the PPS influenced by angle regulation under the TE wave. (c) Plot illustrating the relationship between angle and transmittance at 530 THz. The blue dotted line corresponds to an angle of 30° , the orange line to 60° , and the blue solid line to the frequency of 510 THz, when the medium is arranged $C_2(DC_1)^{12}DC_2A_2(BA_1)^9BA_2C_2(DC_1)^{12}DC_2$. (d) Distribution of the real and imaginary parts of the surface effective impedance. (Since TE and TM waves are completely symmetrical on both sides of 0° , to make the phenomenon more obvious, only TM waves are drawn at -90° and only TE waves are drawn at a positive angle).

transitioning from -46° – 46° to -40.2° – 40.2° . Considering both TE and TM, the visible region shifts from -46° – 46° to -40.2° – 40.2° . Conversely, as d_A gradually increases to 183 nm, the visible region expands. At 510 THz, for TE waves, the visible region expands from -29° – 29° to -31.5° – 31.5° and further extends to -35.4° – 35.4° . Similarly, for TM waves, the visible region broadens from -34° – 34° to -38.6° – 38.6° and further to -42.9° – 42.9° . Considering both TE and TM, the visible region expands from -34° – 34° to -38.6° – 38.6° and further to -42.9° – 42.9° . Therefore, as d_A gradually increases, the visible region also enlarges, while a decrease in d_A leads to a reduction in the angle window.

Examining the influence of d_B on PPS performance, figure 8 portrays a gradual reduction in the visible region within the 510–530 THz range as d_B decreases from 164 nm to 156 nm. Using 530 THz as an example, both TE and TM waves experience a contraction in the visible region, with TE waves narrowing from -38° – 38° to -32.4° – 32.4° and TM waves transitioning from -46° – 46° to -40° – 40° . Considering both

TE and TM, the visible region shifts from -46° – 46° to -40° – 40° . Conversely, with d_B gradually increasing to 175 nm, the visible region expands. At 510 THz, TE waves exhibit an expansion from -29° – 29° to -30.8° – 30.8° , further extending to -32.9° – 32.9° . Similarly, for TM waves, the visible region broadens from -34° – 34° to -38.2° – 38.2° and further to -40° – 40° . Considering both TE and TM, the visible region expands from -34° – 34° to -38.2° – 38.2° and further to -40° – 40° . Consequently, as d_B gradually increases, the visible region enlarges, while a decrease in d_B leads to a reduction in the angle window.

The discussion results of the above four parameters (n_A , n_B , d_A , d_B) are summarized in tables 1 and 2, and the impact of each parameter on PP performance can be clearly seen.

It can be summarized in tables 1 and 2 that for the increase of the four parameters (n_A , n_B , d_A , d_B), the scope of the visible area will gradually increase, and for the decrease of the four parameters (n_A , n_B , d_A , d_B), the scope of the visible area will gradually decrease. The size of the visible area of the PSS can

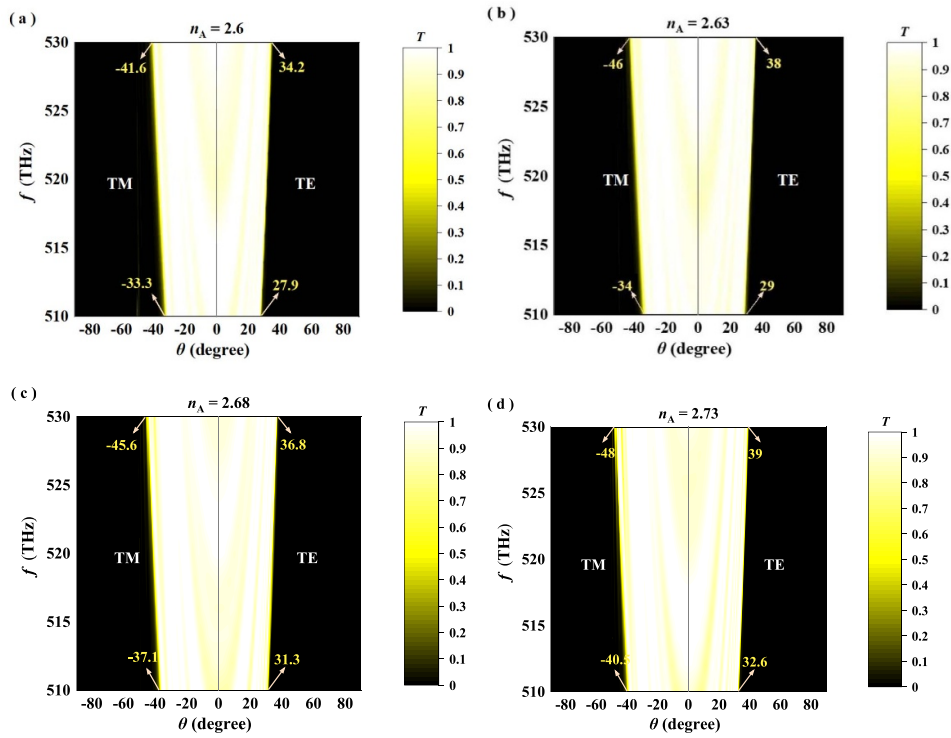


Figure 5. The relationships among transmittance, frequency, and viewing angle under varying refractive indices: (a) $n_A = 2.6$, (b) $n_A = 2.63$, (c) $n_A = 2.68$, and (d) $n_A = 2.73$. (As TE and TM waves exhibit complete symmetry on both sides of 0° , to emphasize the phenomenon more distinctly, TM waves are exclusively illustrated at -90° , while TE waves are exclusively depicted at positive angles).

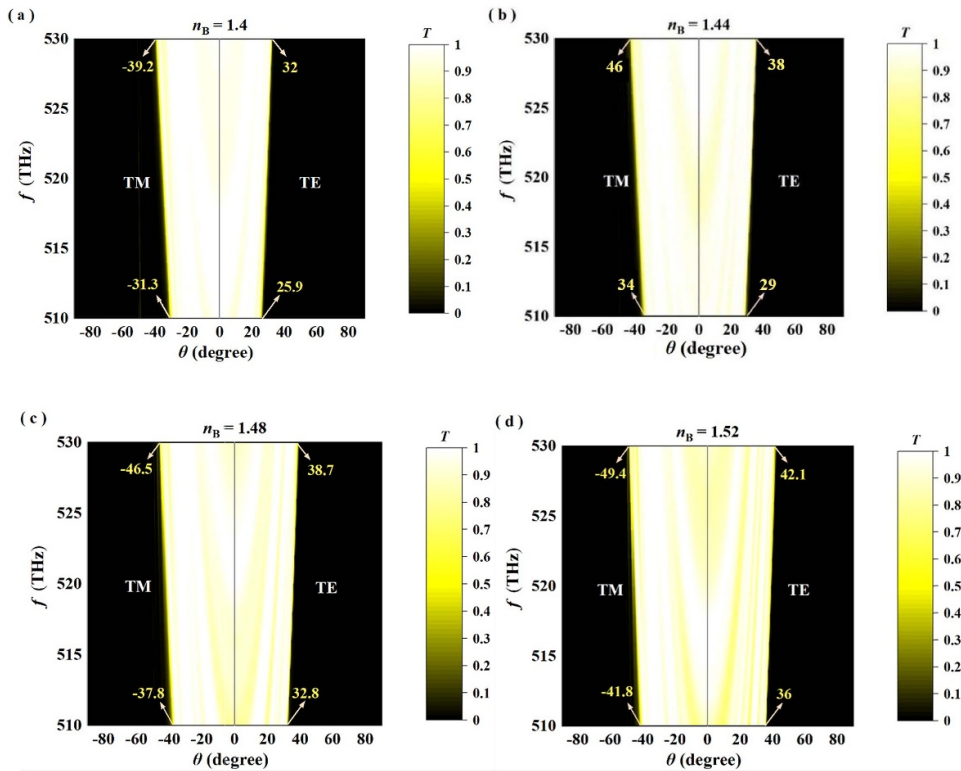


Figure 6. The relationships among transmittance, frequency, and viewing angle under different refractive indices: (a) $n_B = 1.4$, (b) $n_B = 1.44$, (c) $n_B = 1.48$, and (d) $n_B = 1.52$. (Given the complete symmetry of TE and TM waves on both sides of 0° , to highlight the phenomenon more distinctly, TM waves are exclusively depicted at -90° , while only TE waves are illustrated at positive angles).

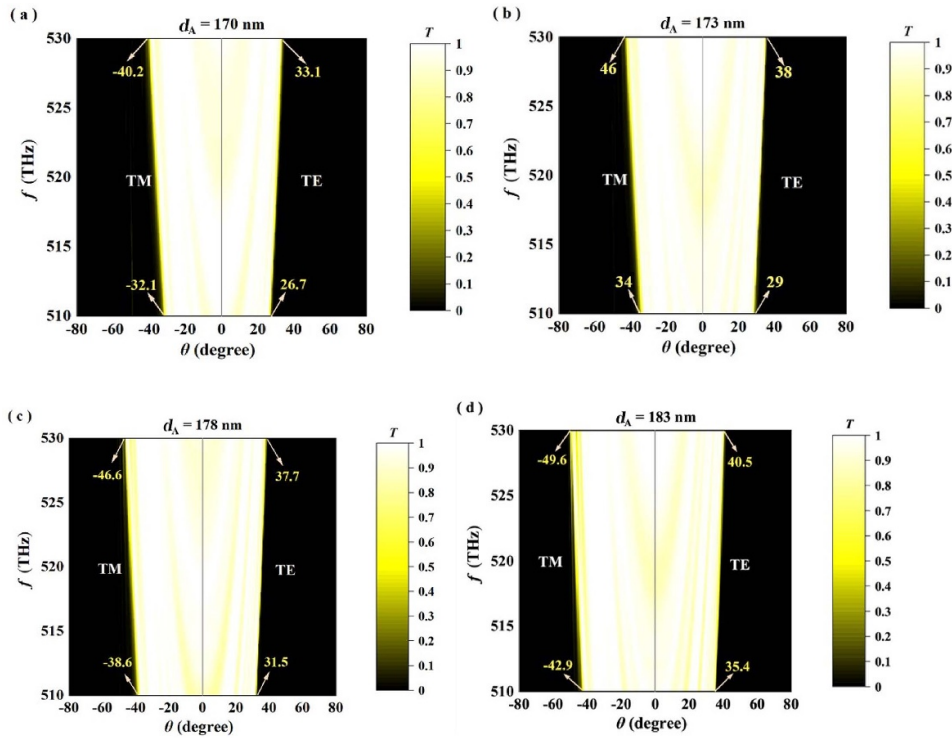


Figure 7. The relationships among transmittance, frequency, and viewing angle under different thicknesses: (a) $d_A = 133$ nm, (b) $d_A = 143$ nm, (c) $d_A = 153$ nm, and (d) $d_A = 193$ nm. (To accentuate the phenomenon's clarity due to the complete symmetry of TE and TM waves on both sides of 0° , TM waves are exclusively depicted at -90° , while only TE waves are illustrated at positive angles).

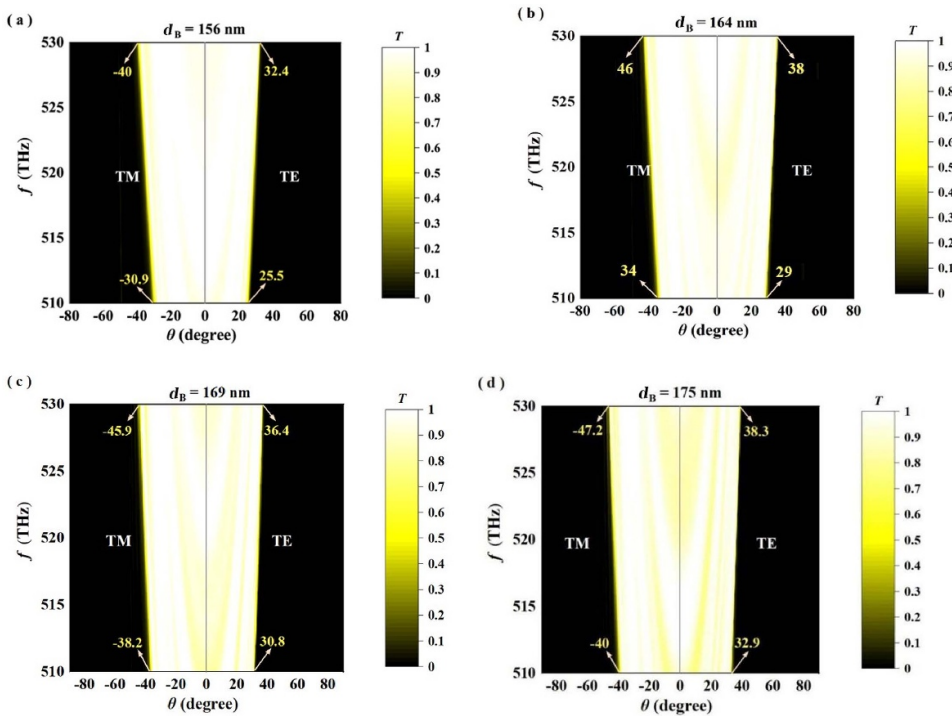


Figure 8. The relationships among transmittance, frequency, and viewing angle under different thicknesses: (a) $d_B = 64$ nm, (b) $d_B = 114$ nm, (c) $d_B = 134$ nm, and (d) $d_B = 184$ nm. (Given the complete symmetry of TE and TM waves on both sides of 0° , for clarity, TM waves are exclusively represented at -90° , while only TE waves are depicted at positive angles).

Table 1. Effects of increasing main parameters on performance.

	Effect of parameter increase on visual area range	Parameter increase visual range (510 THz)	Parameter increase visual range (530 THz)
$n_A = 2.63\text{--}2.6$	Increase	$[-34^\circ, 34^\circ] \sim [-40.5^\circ, 40.5^\circ]$	$[-46^\circ, 46^\circ] \sim [-48^\circ, 48^\circ]$
$n_A = 1.4\text{--}1.52$	Increase	$[-34^\circ, 34^\circ] \sim [-41.8^\circ, 41.8^\circ]$	$[-46^\circ, 46^\circ] \sim [-49.4^\circ, 49.4^\circ]$
$d_A = 173\text{--}183$ nm	Increase	$[-34^\circ, 34^\circ] \sim [-42.9^\circ, 42.9^\circ]$	$[-46^\circ, 46^\circ] \sim [-49.6^\circ, 49.6^\circ]$
$d_B = 164\text{--}156$ nm	Increase	$[-34^\circ, 34^\circ] \sim [-40^\circ, 40^\circ]$	$[-46^\circ, 46^\circ] \sim [-47.2^\circ\text{--}47.2^\circ]$

Table 2. Impact of major parameter reduction on performance.

	Effect of parameter reduction on visual area range	Parameter reduced visual range (510 THz)	Parameter reduced visual range (530 THz)
$n_A = 2.63\text{--}2.6$	Decrease	$[-34^\circ, 34^\circ] \sim [-33.3^\circ, 33.3^\circ]$	$[-46^\circ, 46^\circ] \sim [-41.6^\circ, 41.6^\circ]$
$n_A = 1.4\text{--}1.52$	Decrease	$[-34^\circ, 34^\circ] \sim [-35.6^\circ, 35.6^\circ]$	$[-46^\circ, 46^\circ] \sim [-42.5^\circ, 42.5^\circ]$
$d_A = 173\text{--}183$ nm	Decrease	$[-34^\circ, 34^\circ] \sim [-32.1^\circ, 32.1^\circ]$	$[-46^\circ, 46^\circ] \sim [-40.2^\circ, 40.2^\circ]$
$d_B = 164\text{--}156$ nm	Decrease	$[-34^\circ, 34^\circ] \sim [-30.9^\circ, 30.9^\circ]$	$[-46^\circ, 46^\circ] \sim [-40^\circ, 40^\circ]$

be adjusted by changing four parameters to achieve different angle ranges of PP.

4. Conclusion

Sum up, it achieved a remarkable transmittance of greater than 0.85 in the visible area (-29° to 29°) and 0.1 in the protected area (-90° to -46° and $46^\circ\text{--}90^\circ$), also effectively confines the transition angle range to less than 20° . The anti-reflection performance is influenced by the four parameters (n_C, n_D, d_C, d_D). Different combinations of these parameters yield varying effects. The impact of these parameters primarily involves the transmittance magnitude in the visual area, AS, and transmittance magnitude in the protected area. This groundbreaking innovation transcends the limitations of conventional anti-peep structures [7, 21], successfully surmounting challenges related to low transmittance and an extended visual range, and carries substantial practical value in fields that demand unique perspectives or specific light wave requirements. In the foreseeable future, we anticipate that this technology will play a pivotal role in areas such as PP, information security, military applications, and surveillance systems within high-security environments. Furthermore, this innovative technology may find applications in optical communication, virtual reality, and augmented reality, presenting more advanced and flexible solutions to these domains.

Data availability statement

The data cannot be made publicly available upon publication because they are not available in a format that is sufficiently accessible or reusable by other researchers. The data that support the findings of this study are available upon reasonable request from the authors.

ORCID iD

Hai-Feng Zhang  <https://orcid.org/0000-0002-9890-8345>

References

- [1] Winkler T and Rinner B 2014 *ACM Comput. Surv.* **47** 1–42
- [2] Liu M et al 2012 *Nature* **487** 345–8
- [3] Padilla-López J R, Chaaaroui A A and Flórez-Revuelta F 2015 *Expert Syst. Appl.* **42** 4177–95
- [4] Perez A J and Zeadally S 2017 *IT Prof.* **20** 46–56
- [5] Motti V G and Caine K 2015 *Financial Cryptography and Data Security: FC International Workshops, BITCOIN, WAHC, and Wearable, San Juan, Puerto Rico, January 30, 2015, Revised Selected Papers.* (Springer) pp 231–44
- [6] Palmero-Marrero A I and Oliveira A C 2010 *Appl. Energy* **87** 2040–9
- [7] Lim Y J, Kim J H, Her J H, Bhattacharyya S S, Park K H, Lee J H, Kim B K and Lee S H 2010 *Opt. Express* **18** 6824–30
- [8] Choi T H, Lee H W and Ha J U 2023 *Appl. Opt.* **62** 584–91
- [9] Baek J, Kwon Y-H, Kim J C and Yoon T-H 2007 *Appl. Phys. Lett.* **90** 101104
- [10] Li Z and Zhang S 2021 *Optoelectron. Technol.* **41** 228
- [11] Kim S S, Berkeley B H, Park J H and Kim T 2006 *J. Soc. Inf. Disp.* **14** 127–34
- [12] Lim Y W, Yeo M and Lee J 2023 *Opt. Mater. Express* **13** 161–70
- [13] Chen Q, Peng Z, Li Y, Liu S, Zhou P, Gu J, Lu J, Yao L, Wang M and Su Y 2019 *Opt. Express* **27** 12039–47
- [14] Shen Y, Ye D, Celanovic I, Johnson S G, Joannopoulos J D and Soljačić M 2014 *Science* **343** 1499–501
- [15] Vázquez-Lozano J E and Liberal I 2023 *Nat. Commun.* **14** 4606
- [16] Krasnov A 2023 *Opt. Mater.* **135** 113302
- [17] Shen W and Li G 2023 *Laser Photon. Rev.* **17** 2200207
- [18] Dai M, Zhao J, Zhang Y, Li H, Zhang L, Liu Y, Ye Z and Zhu S 2022 *ACS Appl. Mater. Interfaces* **14** 53314–22
- [19] Aburabie J, Eskhan A and Hashaikeh R 2022 *Macromol. Rapid Commun.* **43** 2200172
- [20] Liu C K, Tu C Y, Lin H R, Lim Y J, Kim J H, Her J H, Kang W-S, Lee G-D and Lee S H 2010 *J. Phys. D: Appl. Phys.* **43** 085501
- [21] Liu C K, Tu C-Y, Lin H-R and Cheng K-T 2020 *Opt. Laser Technol.* **121** 105778
- [22] Liu C-K, Chang S-C, Juang Y-S and Cheng K-T 2023 *Opt. Express* **31** 2445–55
- [23] Iizuka H, Engheta N and Sugiura S 2016 *Opt. Lett.* **41** 3829–32
- [24] Xu J, Mandal J and Raman A P 2021 *Science* **372** 393–7
- [25] Hamam R E, Celanovic I and Soljačić M 2011 *Phys. Rev. A* **83** 035806

- [26] Schwartz B T and Piestun R 2003 *J. Opt. Soc. Am. B* **20** 2448–53
- [27] Shi B, Jiang Z M and Wang X 2001 *Opt. Lett.* **26** 1194–6
- [28] Guo J, Chen S and Jiang S 2017 *J. Mod. Opt.* **65** 1–9
- [29] Green D G 1968 *J. Physiol.* **196** 415–29
- [30] Mullen K T 1985 *J. Physiol.* **359** 381–400
- [31] Kooi F L, Alferdinck J and Post D 2005 *Yellow lessens discomfort glare: physiological mechanism (s)* (Shaker Publishing BV)
- [32] Pimputkar S, Speck J S, DenBaars S P and Nakamura S 2009 *Nat. Photon.* **3** 180–2
- [33] Lee Y, Yoon D, Yu S, Sim H, Park Y, Nam Y S and Son J 2022 *Adv. Mater.* **34** 2107650
- [34] Fink Y, Winn J N, Fan S, Chen C, Michel J, Joannopoulos J D and Thomas E L 1998 *Science* **282** 1679–82
- [35] She Y, Liu D, Li J, Yao M, Zheng Y and Wu F 2024 *Phys. Lett. A* **494** 129299
- [36] Munkhbat B, Wrobel P, Antosiewicz T J and Shegai T O 2022 *ACS Photonics* **9** 2398–407
- [37] Tabata M, Adachi I and Fukushima T 2005 *2005 IEEE Nuclear Science Symp. Conf. Record* vol 2 pp 816–8
- [38] Kim G S and Hyun S H 2003 *J. Non-Cryst. Solids* **320** 125–32
- [39] Sasaki T, Mori Y and Yoshimura M 2003 *Opt. Mater.* **23** 343–51
- [40] Marple D T F 1964 *J. Appl. Phys.* **35** 539–42
- [41] Hale G M and Querry M R 1973 *Appl. Opt.* **12** 555–63
- [42] Popoff S M, Lerosey G, Carminati R, Fink M, Boccara A C and Gigan S 2010 *Phys. Rev. Lett.* **104** 100601
- [43] Shlivinski A and Hadad Y 2018 *Phys. Rev. Lett.* **121** 204301
- [44] Lee J W, Seo M A, Sohn J Y, Ahn Y H, Kim D S, Jeoung S C, Lienau C and Park Q-H 2005 *Opt. Express* **13** 10681–7
- [45] Nga D T, Phan A D, Lam V D, Badloe T and Rho J 2023 *Opt. Mater. Express* **13** 2787–97
- [46] Wang H and Li Y P 2001 *Acta Phys. Sin.* **50** 2172–8